Los Alamos NATIONAL LABORATORY EST.1943

LA-UR-15-24743 (Accepted Manuscript)

On shock driven jetting of liquid from non-sinusoidal surfaces into a vacuum

Cherne, Frank Joseph
Hammerberg, James Edward
Andrews, Malcolm John
Ramaprabhu, Praveen
Karkhanis, V.

Provided by the author(s) and the Los Alamos National Laboratory (2016-09-01).

To be published in: Journal of Applied Physics

DOI to publisher's version: 10.1063/1.4934645

Permalink to record: http://permalink.lanl.gov/object/view?what=info:lanl-repo/lareport/LA-UR-15-24743

Disclaimer:
Approved for public release. Los Alamos National Laboratory, an affirmative action/equal opportunity employer, is operated by the Los Alamos National Security, LLC for the National Nuclear Security Administration of the U.S. Department of Energy under contract DE-AC52-06NA25396. Los Alamos National Laboratory strongly supports academic freedom and a researcher's right to publish; as an institution, however, the Laboratory does not endorse the viewpoint of a publication or guarantee its technical correctness.

RESEARCH LIBRARY

LA-UR-15-24743

On Shock Driven Jetting of Liquid from Non-Sinusoidal Surfaces into a Vacuum

F.J. Cherne, [1]J.E. Hammerberg,[1,a] M.J. Andrews,[1] V. Karkhanis,[2] and P. Ramaprabhu[2]

[1]*Los Alamos National laboratory, Los Alamos National Laboratory, 87545, Los Alamos, New Mexico, USA*

[2]*The William States Lee College of Engineering, University of North Carolina at Charlotte, Charlotte, North Carolina, 28223-0001, USA*

Previous work employed Richtmeyer-Meshkov theory to describe the development of spikes and bubbles from shocked sinusoidal surfaces. Here we discuss the effects of machining different two-dimensional shaped grooves in copper, and examine the resulting flow of the material after being shocked into liquid on release. For these simulations a high performance molecular dynamics code, SPaSM, was used with machined grooves of kh_0=1 and kh_0=1/8 where $2h_0$ is the peak-to-valley height of the perturbation with wavelength λ, and $k=2\pi/\lambda$. The surface morphologies studied include: a Chevron, a Fly-Cut, a Square-Wave, and a Gaussian. We describe extensions to an existing ejecta source model that better captures the mass ejected from these surfaces. We also investigate the same profiles at length scales of order 1 cm for an idealized fluid equation of state using the FLASH continuum hydrodynamics code. Our findings indicate that the resulting mass can be scaled by the missing area of a sinusoidal curve with an effective wavelength, λ_{eff}, that has the same missing area. Our extended ejecta mass formula works well for all the shapes considered, and captures the corresponding time evolution and total mass.

[a] Author to whom correspondence should be addressed. Electronic mail: jeh@lanl.gov

I. INTRODUCTION

The term "ejecta" refers to: 1) the removal of mass from a material surface due to the passage of a shock wave over that surface, 2) its subsequent movement through a participating medium, and 3) its ultimate conversion (e.g. recollection or evaporation). We refer to these three distinct steps respectively as "source," "transport," and "conversion." Driven materials are well known (Assay & Bertholf[1], Buttler et al.[2]) to produce a spread of mass scooped out as a shock passes over the surface, forming a jet of small particles. This article concerns itself with mathematical models that describe the process of removing mass, "sourcing", from a surface to a surrounding volume.

Previous research to understand ejecta sources has in most cases focused on experimental characterization, which was then parameterized and used for predictive simulations. This encompassing approach took ejecta experiments that spanned a 20 year period and produced a useful correlation technique. We have taken a different route, based on ejecta phenomena that originate from a Richtmyer-Meshkov-Instability (RMI) that occurs as a shock passes over a roughened interface between two materials of different density. For ejecta the typical Atwood number, $A_t=(\rho_{light}-\rho_{heavy})/(\rho_{light}+\rho_{heavy})$ is close to -1, and Buttler et al.[2] and Dimonte et al.[3] developed RMI based mathematical models for sources of ejecta from liquid/vacuum, liquid/gas, and solid/gas configurations based on the work of Mikaelian[4]. Here we focus on the vacuum case as there is an extensive set of data from Buttler et al.[5-11]. Moreover, in a vacuum $A_t = -1$ and thus downstream measurements of mass released are due solely to the shock passage and RMI. This approach is consistent with the "source" concept for the overall ejecta description given above, and means that we can perform independent "source" and "transport" experiments, and thus de-convolve the physical processes. An added complexity that can occur in applications is a second shock interaction with the surface sometime after the first shock has passed. The difficulty with second shock is that the surface will have already sourced ejecta, and thus the surface may not be well characterized, leaving poorly defined initial conditions. In what follows we seek to give insight into our extended first shock ejecta source model, and the development of a second shock ejecta source model.

Previous research[1-11] has centered on sinusoidal perturbations (grooves). Ejecta source term models, and the flow characteristics for liquid ejecta production, have been produced[2,3,12,13]. There have been a few papers that have looked at the role of non-sinusoidal surface effects in the study of Richtmyer-Meshkov instability theory[4], and understanding experimental ejecta production[1]. Several recently published works using molecular dynamics have focused on the role of ejecta production and most have focused on the velocity and size distribution of the ejected material using copper, tin, aluminum, and lead[14-20]. Li et al.[19] used molecular dynamics to look at the spike tip velocity and the source of the material in the spike tips from different perturbations similar to what we present here but for a material that remained solid on release. The focus of our

paper will be less upon the spike tip velocities but more upon characterizing the mass generated and its relation to the model by Buttler et al.[2]. Few of the simulations report the areal density with the notable exception being the paper by Durand et al.[20] which was presented for tin instead of copper. Here we consider several non-sinusoidal surfaces using molecular dynamics simulations, and larger length and time scale hydrodynamic simulations, to aid in the development of a generalized understanding of the role of various surface structures. We also limit our discussion to the situation for which the material is fluid on release.

Molecular dynamics (MD) has been successfully used to study a variety of shock induced processes including ejecta production, phase transitions, void collapse, and nucleation of defects[14-28]. The first large-scale MD simulations for ejecta were those of Germann et al.[21a] for flat surfaces and later for sinusoidal perturbations[21b]. In the present work, molecular dynamics has been applied to develop an understanding of ejecta production from non-sinusoidal surfaces. Previously published mathematical models, such as those of Dimonte et al.[3] or Buttler et al.[2] were based upon Richtmyer-Meshkov instability theory of sinusoidal surfaces, extended to nonlinear development from the work of Mikaelian[29,30]. In a related work on non-sinusoidal initial surfaces, Asay and Bertholf[1] looked at ejecta production from several different surfaces using a continuum code and compared the results with experimental data. Mikaelian[4] looked at arbitrary shapes, and showed that, in the initial linear regime, the development of spikes and bubbles can be simply described using Fourier series analysis. We show that for complex surface profiles, the associated Fourier power spectrum effectively decays, and a simplified Fourier series analysis provides adequate information to give an initial condition for the longest wavelength in the series representation of the shape that propagates to late-time.

Section II develops a theory of ejecta production based upon the work of Buttler et al.[2]. In section IIIA, we discuss the molecular dynamics techniques and the potential used for the present work. In particular, we consider a constant shock strength for which the material, copper, is melted on the first shock. Specifically, a particle velocity of u_p=2.5 km/s is studied. For comparison and validation purposes, a continuum method is presented in section IIIB. The evolution of the surface morphology is studied for different initial starting configurations that include: Sinusoidal, Chevron, Fly-Cut, Square, and a Gaussian profile. A discussion of the mathematical and the Fourier representation of these shapes is discussed in section IV. Section V presents the computed characteristics of the resulting jets, and introduces a scaling that allows their collapse to form a useful engineering model. Section VI presents our conclusions.

II. THEORETICAL CONSIDERATIONS

Buttler et al.[2] developed an ejecta source model applicable at a metal-vacuum interface as a special limiting case of the RM instability $A_t \to -1$. The authors[2] developed an expression for the initial peak bubble/spike growth rates under ejecta conditions and for large initial amplitudes as:

$$\dot{\eta}_0^{b,s} = F_l F_{nl}^{b,s} \left| k h_0 \Delta u \right| \quad . \tag{1}$$

In Equation (1), $F_l = 1 - \Delta u / 2u_s$ is a linear shock compression factor (for the perturbation amplitude), while $F_{nl}^{b} = 1/(1 + kh_0/6)$ and $F_{nl}^{s} = 1/(1 + (kh_0/2)^2)$ are nonlinear correction factors relevant to bubbles and spikes respectively. Furthermore, u_s and Δu are the shock velocity and free-surface velocities, respectively, in the frame of reference in which the interface is initially at rest. According to [9] the surface of the liquid metal, envisaged in Figure 1, may be conveniently described as the shock driving bubbles that in turn excavate material mass out from the surface and into the spikes. The theory suggested originally by [29], and adopted by [2], produces two key parameters, namely the bubble tip velocity $\dot{\eta}^b$, and the spike tip velocity $\dot{\eta}^s$; the formulas for these parameters can be summarized as:

$$\begin{aligned} \dot{\eta}^b &= \frac{\dot{\eta}_0^b}{1 + \frac{3}{2}\dot{\eta}_0^b k t} \\ \dot{\eta}^s &= \sqrt{3}\dot{\eta}_0^s \end{aligned} \quad . \tag{2}$$

In what follows we address bubble evolution from which we develop a theory of ejecta source mass production for a variety of shapes. The subscript "0" refers to values associated with the initial state (i.e. immediately after the shock has passed), and wavenumber $k = 2\pi/\lambda$ where λ is the wavelength of the initial perturbation. Of particular interest in Equation (2) for the bubble is the inverse time decay of the bubble velocity, and that shorter wavelengths (higher wavenumbers) decay faster. In contrast, the spike attains a steady terminal velocity. The difference lies in the low drag and added mass of the spike compared with the bubble, which causes the bubble to slow inversely with time. The areal mass (mass per unit area A) excavated and then ejected by the bubble is readily computed from Equation (2) as:

$$M(t)/A = \rho \int_0^t \dot{\eta}^b(t') S_f(t') dt' = m_0 \ln\left(1 + \frac{t}{\tau}\right) \quad , \tag{3}$$

where S_f is a shape factor that is taken as 1 in Equation (3), $m_0=\rho\lambda/3\pi$, and $\tau = \lambda / (3\pi\dot{\eta}_0^b)$. Equation (3) is the basic ejecta source model.

We consider two useful extensions. The first is to take a parabolic shape factor, motivated by the computational results presented here and the experiments of Buttler et al. [2,5-11].After inspection of the MD results we observed that the apparent shape of the bubble was that of a parabola. Of course this is only an approximation but it is also commensurate with potential models for non-linear bubble growth such as those that originated with Layzer [31].

$$m(t) = \frac{M(t)}{A} = \frac{\rho}{\lambda}\int_0^t \left(\int_{-L_B}^{L_B} \dot{\eta}^b(t')(1-(\frac{x}{L_B(t')})^2)\,dx \right) dt' = \frac{\rho}{\lambda}\int_0^t \dot{\eta}^b(t')\frac{4}{3}L_B(t')dt' \quad . \tag{4}$$

The second is to assume that the volume flux through the initial free-surface position is conserved, giving:

$$2(L_B + L_s) = \lambda \quad and \quad \dot{\eta}^b L_B = \dot{\eta}^s L_s \quad . \tag{5}$$

Here L_B and L_s are the half-widths of the bubble and spike respectively. Inserting Equation (5) into Equation (4) and after some algebra we find:

$$m(t) = \frac{2}{3} m_0 \ln(1+\frac{t}{\beta\tau}) \quad with \quad \beta = 1+\frac{1}{\sqrt{3}}\frac{F_{nl}^b}{F_{nl}^s} \quad . \tag{6}$$

The m_0 and τ parameters in Equation (6) are just those of Equation (3), so it is evident that the parabolic shape reduces the areal mass by 2/3 and lengthens the time scale as β. In the simulation work that follows we examine the accuracy of these formulas. A differential expression for Equation (6) more suitable to implementation in a hydrodynamic computer code is given below in Equation (12).

One further extension can be made to Equation (4) and is associated with the assumption in the Buttler[2] result that takes the initial bubble amplitude η_0^b , as zero (but not its velocity). The expression for $\dot{\eta}_0^b(t)$ of Equation (2) corresponds to a time origin for shock breakout at the bottom of the perturbation (valley). We assume that it takes time Δt from shock breakout for the peak/valley to decrease/increase by the compressed bubble/spike amplitude, $\tilde{\eta}_0^b = \frac{1}{2}(h_0 + (1-\frac{\Delta u}{u_s})h_0) = h_0 F_l$, and thus the interface to become substantially flat, then Δt is determined by:

$$\tilde{\eta}_0^b = \int_0^{\Delta t} \dot{\eta}^b(t)\,dt \ . \tag{7}$$

Using the bubble velocity of Equation (2) in Equation (7) gives:

$$\frac{\Delta t}{\tau} = e^{\frac{3}{2}k\tilde{\eta}_0^b} - 1 = e^{\frac{3}{2}kh_0 F_l} - 1 \ . \tag{8}$$

Then the *m(t)* of Equations (4) and (8) is given by:

$$m(t) = \frac{2}{3} m_0 \, ln\left[1 + \frac{(t - \Delta t)}{(\beta + \frac{\Delta t}{\tau})\tau} \right] \qquad (t \geq \Delta t) \ . \tag{9}$$

As one might expect, it is evident that for small kh_0 there is little change to Equation (6) and that in the limit $kh_0 \to 0$ Equation (9) reduces to Equation (6). However the effect is relevant for the kh_0=1 case considered here, and for second shock considerations described in the following paragraph.

For later comparisons, a model implementation would use the differential form of Equation (4) with the initial velocity obtained from Equation (2) as:

$$\dot{\eta}_{0,\Delta t}^b = \frac{\dot{\eta}_0^b}{1 + \frac{3}{2}\dot{\eta}_0^b k \Delta t} = \frac{\dot{\eta}_0^b}{1 + \frac{\Delta t}{\tau}} \ , \tag{10}$$

and an effective "reduced" velocity given by:

$$\dot{\eta}_{\Delta t}^b(t) = \frac{\dot{\eta}_{0,\Delta t}^b}{1 + \frac{3}{2}\dot{\eta}_{0,\Delta t}^b kt} \qquad \text{and} \qquad \dot{\eta}_{\Delta t}^s = \sqrt{3}\dot{\eta}_{0,\Delta t}^s \ , \tag{11}$$

where t corresponds to the time from the flat interface. The associated differential form of Equation (4) becomes:

$$\frac{dm(t)}{dt} = \frac{4}{3}\frac{\rho}{\lambda}\dot{\eta}_{\Delta t}^b(t) L_B(t) = \frac{2}{3}\rho \dot{\eta}_{\Delta t}^b \frac{\dot{\eta}_{\Delta t}^s}{\dot{\eta}_{\Delta t}^b + \dot{\eta}_{\Delta t}^s} \ . \tag{12}$$

How then to mathematically describe ejecta formation from second shock? The fundamental problem is to know what the surface profile might look like at second shock, a difficult problem for which no experimental data has been collected. Our approach has been to state a hypothesis for the surface condition at second shock, and then explore its validity. The hypothesis is: "It is the longest wavelength and its amplitude on the surface of the material that determine most of the mass

source." The hypothesis is motivated by the observation above that short wavelength (high wavenumber) perturbations decay quickly (see Equation (2)), and leave longer wavelengths to excavate most of the mass (see Equations (3) or (6)). One immediate consequence is that shapes with similar wavelengths and amplitudes will source similar areal masses. To study the correctness of the hypothesis the work described below has investigated five different shapes, namely, Sinusoidal, Chevron, Fly-Cut, Square-Wave and Gaussian.

If the different shapes produce similar areal masses then we posit that at second shock we may take the amplitude of the surface bubble perturbations as they evolve after first shock as initial conditions at second shock, with the wavelength being that of the longest one used for the first shock source, and the amplitude taken as half the bubble depth. Moreover, in principle, the argument for second shock applies to subsequent shocks and thus provides a more general framework.

III. NON EQUILIBRIUM MOLECULAR DYNAMICS AND CONTINUUM MODELING OF A RICHTMYER-MESHKOV INSTABILITY

A. Non Equilibrium Molecular Dynamics

Molecular dynamics has been successful in elucidating the physics of interface instabilities such as Rayleigh-Taylor[32,33] and Richtmyer-Meshkov[14-21]. Here we examine the effect of surface shape beyond single wavelength perturbations for ejecta produced by a Richtmyer-Meshkov instability in a liquid metal, copper. To capture the dynamics of the system, continuum methods rely on constitutive relations for the equation of state, yield strength, and surface tension to describe the shock wave processes. Molecular dynamics on the other hand relies on a microscopic interatomic potential that reproduces the atomic forces that lead to the constitutive and dynamical properties of materials. For the Richtmyer-Meshkov instability the molecular dynamics simulations we present are sufficiently large to examine the early time evolution of the surface as the shock breaks out, as well as the later time evolution of the material.

The molecular dynamics simulations presented here were based on an Embedded Atom Method (EAM) potential[34,35], developed by Voter and Chen[36,37]. This many body potential reproduces the elastic, plastic, and defect properties of copper as a function of compression and temperature[25] for the regimes of interest here. Indeed, the dynamic compression curve matches the experimental liquid Hugoniot states. Although the liquid melt transition for this copper potential on the Hugoniot is lower[38] than the experimental melt transition[39], the dynamical properties in the fluid state are reasonably accurate. For these simulations we construct an fcc lattice of copper atoms oriented with the shock direction along the <111> axis. Typical simulations consisted of about 60 million atoms, constituting a thin slab of material 257 nm x 2.67 nm x 1101.6 nm. Periodic

boundary conditions were applied in the directions transverse to the shock. The machined surface was along the x-direction making the principal wavelength λ, equal to 257 nm. A highly efficient, parallel molecular dynamics code, SPaSM[40-42] was used for the molecular dynamics simulations. The time step used was 2.5 fs. A random set of velocities was applied to each individual atom, such that the initial temperature of the simulation was 300 K. The atoms were impacted by a reflective piston boundary resulting in a shock wave that propagated through the material. The piston velocities used generated a particle velocity of u_p=2.5 km/s and a corresponding peak pressure of 161 GPa. At this pressure the copper is in the melted/fluid state, and remains so on release.

B. Continuum simulations using FLASH[43]

The simulations described in this section were performed using the astrophysical FLASH[43] code, developed by the FLASH center for computational sciences at the University of Chicago. The numerical method employed in FLASH is the 2nd order Piecewise Parabolic Method (PPM) to solve the Euler equations. PPM has been demonstrated[44] to be well suited to describing flows involving contact discontinuities such as sharp material interfaces and shocks. FLASH is also equipped with an Adaptive Mesh Refinement (AMR) capability, so that mesh resources are concentrated in regions of large gradients in the primary variables. FLASH is a massively parallel code, with demonstrated scaling performance over hundreds of thousands of processor cores, and across multiple computing platforms. In FLASH, an ideal gas equation of state capable of handling multiple species calculates the thermodynamic properties of an ideal, gamma law fluid.

In our continuum simulations we have adopted the approach of [3] to model metallic ejecta with an equivalent γ-law fluid. In the instance of shock-driven jetting of material from perturbed surfaces, the response of a metal to shock loading can be described using a linear u_s-u_p relation:

$$u_s = c_0 + s u_p \tag{13}$$

Here, u_s is the incident shock speed, while u_p is the particle (piston) velocity behind the shock, c_0 is the bulk sound speed in the metal, and s is a constant. Dimonte et al [3] estimated that for weak shocks, the relationship between the shock speed and the particle velocity in a γ-law fluid simplifies to:

$$u_s = \sqrt{\frac{\gamma_A P_0}{\rho_A}} + \left(\frac{\gamma_A + 1}{4}\right) u_p \tag{14}$$

Equation (14) may be taken to be the γ-law analog of Equation (13), with $c_0 = \sqrt{\frac{\gamma_A P_0}{\rho_A}}$, and $s = \frac{\gamma_A + 1}{4}$. By comparing parametric plots of P, u_s and density vs. u_p, obtained from simulations of a metal described by a Mie-Gruneisen EOS and a γ-

law fluid, Dimonte et al. [3] concluded that the behavior of copper under explosive loading may be approximated by an ideal fluid with ρ_A = 8.93 g/cm^3, and γ_A = 3.0. Specifically, the choice of γ_A = 3.0 was found to reproduce the hydrodynamic response of copper (to within 7%) over the range u_P = 0 – 5 km/s, although the temperature response was not captured due to differences in the EOS. Thus, for the continuum simulations described here, we adopt the following approach to approximate the hydrodynamic response of shock-loaded copper. First, we estimate the incident shock speed u_s from Equation (14) for a particle velocity of u_p = 2.5 km/s employed in the MD simulations. The continuum simulations were then initialized with an initial shock with strength Mach number, $Ma \sim 2.5$ matching the shock properties used in MD. In FLASH, the light fluid was chosen to be air with γ_B = 5/3 and ρ_B = 1.22x10^{-3} g/cm^3, while the copper-equivalent fluid had ρ_A = 8.93 g/cm^3, and γ_A = 3.0. The corresponding particle velocity from the Rankine-Hugoniot jump conditions is 612.53 cm/s. The density of the shocked region is 15.4 g/cm^3, while the corresponding release density for these conditions is 7.57 g/cm^3. Using continuum simulations, we have investigated shock-driven jetting arising from initial perturbations with Sinusoidal, Chevron, Fly-Cut, Square-Wave and Gaussian forms. The initial non-dimensional perturbation amplitudes employed were kh_0=1 and 1/8 and the simulations were run to a time of t/τ=65 and t/τ=44.1 respectively. The perturbation wavelength was chosen to be λ=1 cm for all initial waveforms. To observe the late-time nonlinear development of imposed perturbations, the 2D simulation domain had an aspect ratio of 40 for kh_0=1 and 80 for kh_0=1/8 (corresponding to t/τ=65 and 44.1 respectively). An Adaptive Mesh Refinement (AMR) level of 6 corresponding to an equivalent uniform mesh resolution of 256 zones / λ was employed in the continuum simulations.

Figure 1 is a schematic of the problem configuration used in the numerical simulations reported here, where we have adopted the nomenclature suggested by Mikaelian[45] to delineate shocked and unshocked regions. The pressure in region 3, corresponding to an incident shock strength of Ma=2.5, was initialized to be 8.9x10^5 Pa.

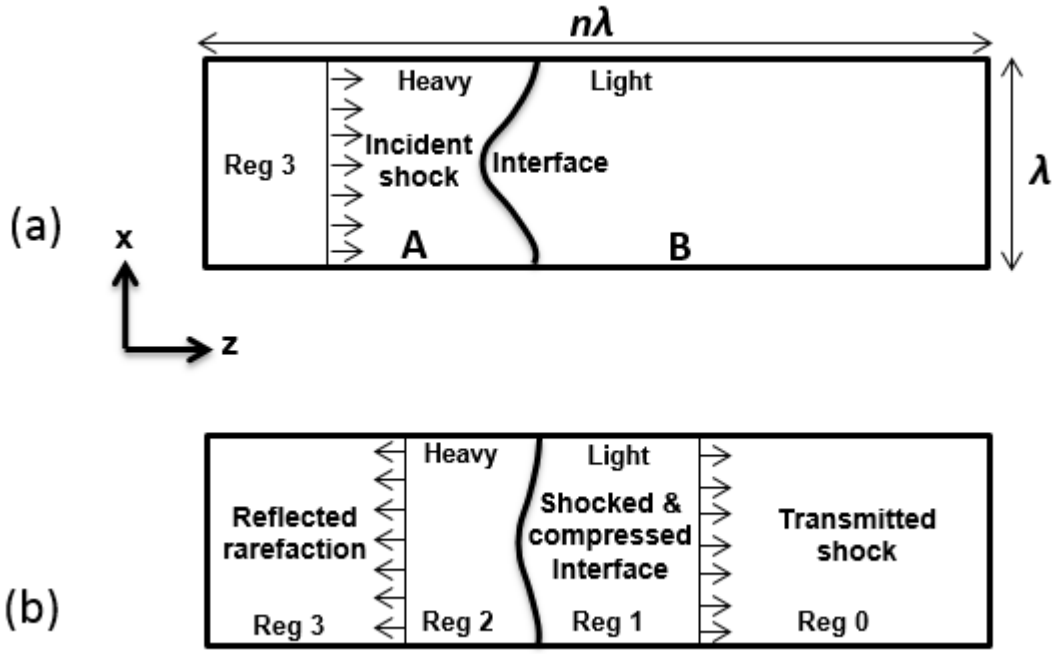

FIG. 1. Schematic of the computational domain showing the problem configuration and nomenclature adopted from [45]. (a) initial condition, (b) configuration after shock-interface interaction.

IV. SURFACES STUDIED

Overview

Surface profiles were constructed at the end of a single crystal using the expressions below. We recognize that some of these profiles may be difficult to manufacture due to their complexity, yet within the molecular dynamics and continuum simulation cell the material ejected from these can be studied to determine isolated geometrical effects. In all of the simulations presented below the kh_0 was held fixed at a value of 1 or 1/8. A value for h_0 was defined as half the total height between the machined surface groove top and bottom. All shapes were constructed about the centerline axis of symmetry, as shown in Figure 2.

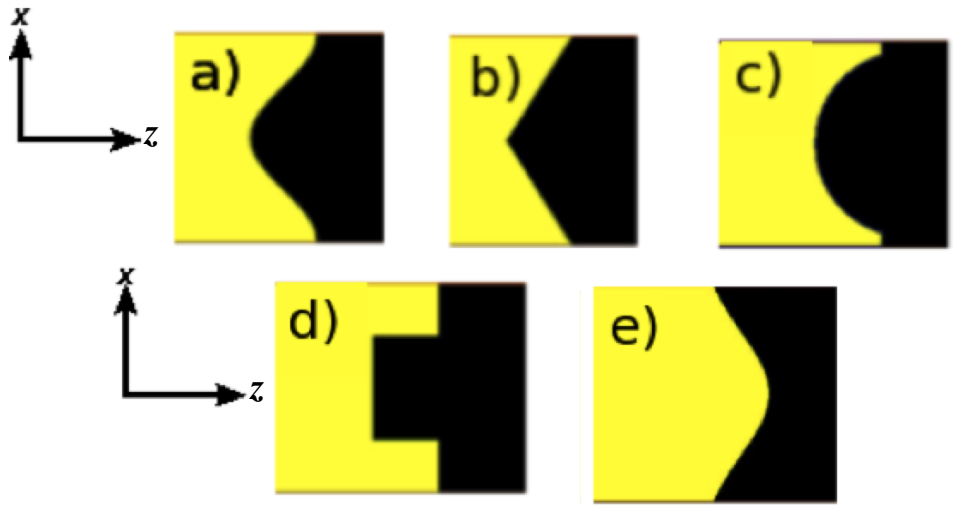

FIG. 2. The shapes described by these functions. a) Sinusoidal, b) Chevron, c) Fly-Cut, d) Square-Wave, and e) Gaussian.

Since the profiles are even periodic functions in x we can use a Fourier cosine series representation. The Fourier cosine series can be generalized as:

$$f(x) = a_0 + \sum_{n=1}^{\infty} a_n \cos(k_n x) \tag{15}$$

where $k_n=(2\pi/\lambda)n$. Mikaelian[4] has defined an "asymptotic-shape" that describes the RM linear growth instability of the perturbation. According to Mikaelian[4] the "asymptotic-shape" for a particular profile is related to the above Fourier series as:

$$f_{asympt}(x) = \sum_{n=1}^{\infty} k_n a_n \cos(k_n x) \tag{16}$$

We note that there are special cases where the above series may not converge, namely, when the a_n values decay as $1/n$, then $k_n a_n$ would be a constant value, and indeed, this is the case for several of the profiles, and may be observed in the resulting surface structure.

The linear RM instability amplitude growth formula for a wavenumber k is, $\eta^k(t)=\eta_0(1+\Delta V k A_t t)$, where ΔV is the velocity of the spike/bubble relative to the free surface, A_t is the Atwood number (defined as $(\rho_g-\rho_s)/(\rho_g+\rho_s)$) where ρ_g and ρ_s are the density of the gas and the solid, respectively), taking a value of -1 for solid shocked into a vacuum, t is time, and

η_0 is the initial sinusoidal amplitude. Applying this to each of the Fourier terms gives a shape that initially develops (with a_0=0) as:

$$\eta(x,t) = \sum_{n=1}^{\infty} a_n \cos(k_n x) + \Delta V A_t t \sum_{n=1}^{\infty} k_n a_n \cos(k_n x) \tag{17}$$

It is evident that the notion of an "asymptotic shape" derives from the development of the second term on the right hand side of Equation (17). However, we note that this is a "linear" R-M evolution, and so as a wave evolves we should expect a different shape from a cosine. Mikaelian [4] also notes that at points where there are discontinuities in the original function, "kink-singularities" form, and are affected by such effects as nonlinearity, compressibility, viscosity, surface tension, strength, etc. For molecular dynamics, these material properties are all included in the simulations through the potential.

In the following we provide the functional representation of the surface and then its Fourier cosine series representation. In some cases, namely for the circular based profiles, the series expansion assumes particular values for the radius, wavelength, and height of the machined well. Our objective with these functions is to develop an understanding for the principal mode responsible for ejecta formation, and the resulting velocities.

Sinusoidal

The simplest, and the standard surface used, to study Richtmyer-Meshkov instability is that of a sinusoid, namely, $h(x) = -h_0 \cos(2\pi x/\lambda)$ and $f_{asympt} = -h_0 k \cos\left(\frac{2\pi x}{\lambda}\right)$. The simulation surface is shown in Figure 2a.

Chevron

This profile could be obtained from a machining process where v-notched grooves were left in the surface. It is also one of the simpler functions for Fourier series representation, and is shown in Figure 2b. The Chevron surface is represented by a periodic representation, and its Fourier cosine series representation is given by:

$$h(x) = \frac{4h_0}{\lambda} |x| - h_0 \qquad -\frac{\lambda}{2} \le x \le \frac{\lambda}{2} \tag{18}$$

and

$$h_f(x) = -\frac{8h_0}{\pi^2} \sum_{n=0}^{\infty} \frac{1}{(2n+1)^2} \cos\left(\frac{2\pi(2n+1)x}{\lambda}\right) \tag{19}$$

We note that in Equation (19) the pre-factor decays as the inverse of the square of the odd coefficients, and also that the asymptotic shape function is given by:

$$f_{asympt}(x) = -\frac{16h_0}{\pi}\sum_{n=0}^{\infty}\frac{1}{(2n+1)}\cos\left(\frac{2\pi(2n+1)x}{\lambda}\right) \tag{20}$$

Fly-Cut

The Fly-Cut shape could be manufactured by the tip of a fly-cutter machining off material at a depth less than the radius of curvature of the machine tool tip. However, as will be evident from the results, the Fly-Cut also closely resembles the late-time evolved shape of all the shapes considered, and as such is a canonical case as an initial condition at second shock. Evaluation of the Fourier cosine coefficients for circle-based shapes is complicated because it involves evaluation of the integral:

$$a_n = \frac{2}{\lambda}\left[\int_0^b\left(Z_0 \pm \sqrt{R^2 - x^2}\right)\cos\left(\frac{2\pi nx}{\lambda}\right)dx + \int_b^{\lambda/2} h_0\cos\left(\frac{2\pi nx}{\lambda}\right)dx\right] \tag{21}$$

where *b* is the intersection of the circle with the flat surface based on the depth of the groove, namely, $\pm\sqrt{2Rh_0 - h_0^2}$, and Z_0 is the translation along the axis of symmetry for the desired circle center. The a_n values oscillate and decay ~ 1/n. The above integral is readily evaluated numerically for a given λ and h_0. We evaluate the Fourier series representation of the above integral for the special case $kh_0 = 1$ below.

This shape is perhaps the closest to a machined surface, Figure 2c. Fly-Cut machine tools consist of a cutting angle with a semicircular section at the tip. The actual functions that produce this shape are given by the following expressions:

$$h(x) = \left\{\begin{array}{cc} h_0 & -\lambda/2 \le x \le -\sqrt{R^2 - ((R-h_0)-h_0)^2} \\ R - h_0 - \sqrt{R^2 - x^2} & -\sqrt{R^2 - ((R-h_0)-h_0)^2} \le x \le \sqrt{R^2 - ((R-h_0)-h_0)^2} \\ h_0 & \sqrt{R^2 - ((R-h_0)-h_0)^2} \le x \le \lambda/2 \end{array}\right\} \tag{22}$$

where *R* is the radius of the tip of the cutter and to generate the series, $R = 2.2h_0$. The Fourier cosine series is:

$$\begin{aligned} h(x) = {} & 0.140274 - 1.11995\cos(x) + 0.162593\cos(2x) + 0.104506\cos(3x) - \\ & 0.126311\cos(4x) + 0.0523246\cos(5x) + 0.0221736\cos(6x) - \\ & 0.0501894\cos(7x) + 0.032069\cos(8x) + 0.00325706\cos(9x)... \end{aligned} \tag{23}$$

and

$$f_{asympt}(x) = -1.11995\cos(x) + 0.325186\cos(2x) + 0.313518\cos(3x) - 0.505244\cos(4x) + 0.261623\cos(5x) + 0.1330416\cos(6x) - 0.3513258\cos(7x) + 0.256552\cos(8x) + 0.02931354\cos(9x)... \quad (24)$$

Square-Wave

This shape, Figure 2d, is not feasibly machined but it is interesting from a modal analysis perspective, and as a limiting case with a step as opposed to a finite gradient. The functional representation of this shape is given by:

$$h(x) = \begin{Bmatrix} h_0 & -\lambda/2 \le x \le -\lambda/4 \\ -h_0 & -\lambda/4 \le x \le \lambda/4 \\ h_0 & \lambda/4 \le x \le \lambda/2 \end{Bmatrix} \quad (25)$$

The Fourier cosine series representation is:

$$h(x) = \sum_{n=1}^{\infty} \frac{4h_0}{n\pi} \sin\left(\frac{n\pi}{2}\right)\cos\left(\frac{2n\pi x}{\lambda}\right) \quad (26)$$

The Fourier coefficients decay as 1/n and oscillate between positive and negative numbers. This is in contrast to the Chevron coefficients that decay as $1/n^2$ for all odd values of n. The longer decay for a Square-Wave may contribute to regions of very high strain rates as the perturbation evolves, namely, the corners of the square well.

The "asymptotic" shape function is:

$$f_{asympt}(x) = \sum_{n=1}^{\infty} \frac{8h_0}{\lambda} \sin\left(\frac{n\pi}{2}\right)\cos\left(\frac{2n\pi x}{\lambda}\right) \quad (27)$$

where this expression does not converge at high values of n, but recall that this result relates to a linear analysis of the evolution.

Gaussian

The motivation for studying the Gaussian surface (Fig. 2e) was that it may best approximate a post-shocked surface profile after a Richtmyer-Meshkov instability inverts. The functional representation of a Gaussian is given by:

$$h(x) = 2h_0 e^{\left(\frac{-x^2}{2c^2}\right)} \quad (28)$$

where h_0 and c are the height and width of the Gaussian spike respectively. Unlike the former profiles, where we have specified the functional axis to be the midpoint between the top and the bottom of the excavated well, here the axis is from the flat surface. The integration of this function to determine the Fourier coefficients is significantly simplified:

$$a_0 = \frac{2h_0 c\sqrt{2\pi}}{\lambda} Erf\left(\frac{\lambda}{2c\sqrt{2}}\right) \tag{29}$$

and

$$a_n = \frac{2h_0 c\sqrt{2\pi}}{\lambda} e^{-\frac{2cn^2\pi^2}{\lambda^2}} \left(Erf\left(\frac{\lambda^2 - 4ic^2 n\pi}{2c\lambda\sqrt{2}}\right) + Erf\left(\frac{\lambda^2 + 4ic^2 n\pi}{2c\lambda\sqrt{2}}\right)\right) \tag{30}$$

From examination of the expression in Equation (30) it is evident that the real portion of a_n decays as $\sim e^{-n^2}$, implying that the first Fourier coefficient would be the dominant mode.

V. DISCUSSION AND RESULTS

We start by discussing the results from molecular dynamics simulations, consisting of a time series for averaged material properties taken from slices of thickness 2.67 nm parallel to the shock front. Initial wavelengths and amplitudes are given in Tables Ia and Ib. Material properties include density, potential energy, velocity in the compression direction, temperature, and stress (longitudinal and shear). Initially the material density is that of a single crystal throughout the sample. The post-shock density was determined from a non-"machined" crystal by inspecting the density after the shock wave released from the free surface. At any given point in time *t,* the bubble (spike prior to inversion) interface was defined as the location along the single crystal where the density was 98.5% of the release density, ρ_{rel} (90% for FLASH simulations). In these simulations with a piston velocity of 2.5 km/s, the release density was 7.92 g/cm^3. Consistent with the theoretical work described above, the bubble height $\eta^b(t)$, was defined as the relative position of the bubble with respect to a free surface, $z^{fs}(t)$, for a system without any machining. For our purposes, we defined the free surface as the location where the excavated mass equaled the mass in the spike, namely:

$$\int_{z^{b,98.5\%}}^{z^{fs}(t)} (\rho_{rel} - \rho(z))dz = \int_{z^{fs}(t)}^{\infty} \rho(z)dz \tag{31}$$

where $\rho(z)$ is the calculated average density of a thin slab of material at location z. The average density results from the sum of mass of each atom present within the volume of material, $L_x * L_y * dz$ at location z, where L_x and L_y are the transverse dimensions of the simulation volume and dz is the increment in the shock direction. An iterative process was used to determine the free surface position, $z^{fs}(t)$. The difference between $z^{b,98.5\%}$ and z^{fs} is the bubble height, $\eta^b(t)$. The ejected areal mass was determined from the right hand side of Equation (31). Figure 3 shows schematically a density profile at time t, that has been analyzed using the above procedure.

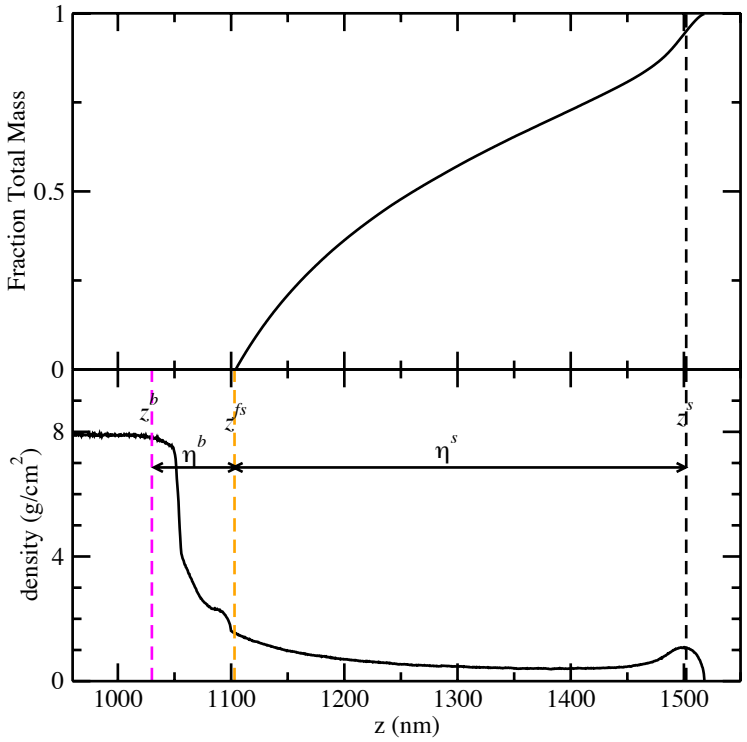

Figure 3. Density and percent mass integral determining the spike position from MD simulations. The vertical dashed lines are projections of the bubble, free-surface, and spike positions.

The determination of the bubble location, $z^{98.5\%}$, is sometimes complicated by either the narrowness of the well or defect structures present after the shock wave has passed through the machined surface. We have minimized this effect by making the density measurements over the middle and outer portions of the simulation, defined as $|x| \le \lambda/4$ and $|x| \ge \lambda/4$ respectively. This partitioning of the profile data provides a more accurate determination of the 98.5 % density position. This same technique was used with the FLASH simulations.

Figure 4 shows snapshots of the resulting surfaces from each of the shapes at a time of 300 ps from the initiation of the shock in the simulation with kh_0=1. This time corresponds to t/τ= 16.77, where the decay time scale is given by $\tau = \lambda / (3\pi\dot{\eta}_0^b)$ and t is the time from the formation of a flat interface. The red line corresponds to the free surface position and conveniently

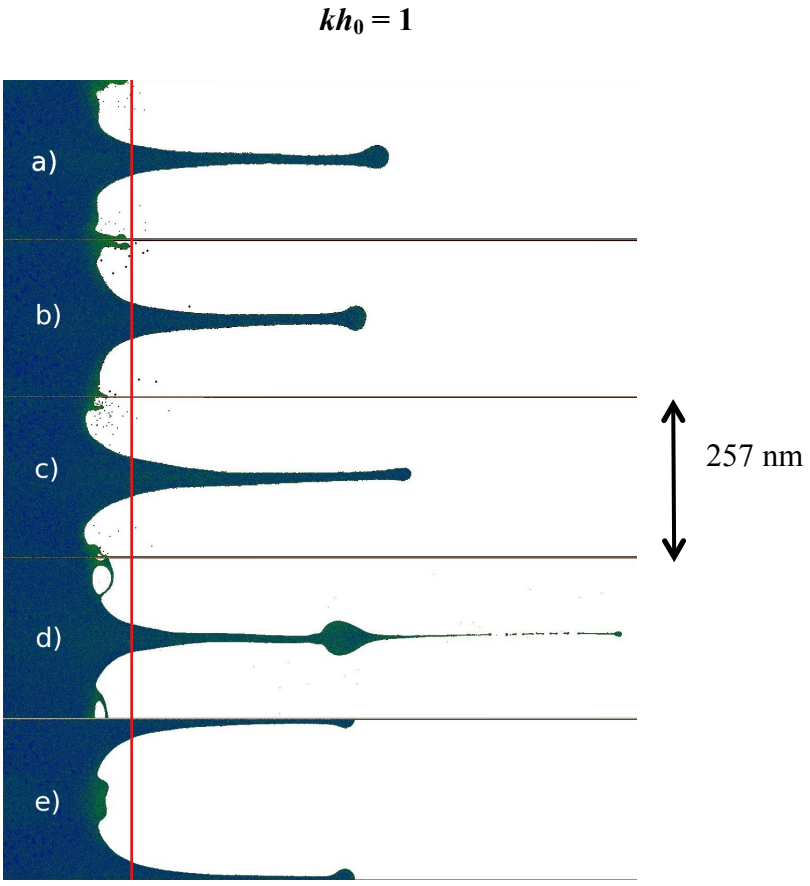

FIG. 4. The evolution of the shapes for the SPaSM Cu simulations at $t/\tau = 16.77$ for each of the machined surfaces at a $u_p = 2.5$ km/s and $kh_0 = 1$. a) Sinusoidal, b) Chevron, c) Fly-Cut, d) Square-Wave, and e) Gaussian.

illustrates how the different profiles evolve the bubble shape. The set of images also illustrates how the morphology of the bubble surface contributes to the evolution of the spike. The bubble penetration and shape are the important observations from these figures, as the bubble excavates mass into the spikes. Qualitative comparison of the bubble profiles across the five shapes reveals a similarity of penetration depth and overall shape, that suggests there is a generality to the development associated with a single mode evolution (i.e. there appears to be no mode coupling from the underlying initial condition). Inspection of the jets in the figure reveals several features that need to be carefully considered. In particular the Sinusoidal, Chevron, and Fly-Cut shapes show no sign of spike breakup, but this is deceptive as there is no participating medium and so the aerodynamic forces that would cause breakup in applications are not treated here. However, the square-wave has a bulbous region just behind a broken spike. This bulbous region occurs when the shock interacts with the right angle at the

base of the well sending a jet of material angled at 45 degrees toward the center, but again may not be relevant to a practical situation where aerodynamic forces will quickly atomize such structures.

Initial wavelengths and amplitudes for the FLASH simulations are given in Tables IIa and IIb. Figure 5 shows density plots from the FLASH simulations for kh_0=1 at a length scale 40,000 times larger for the same value of t/τ as in Figure 4 (t/τ= 16.77) for Sinusoidal, Chevron and Square Wave profiles with remarkably good agreement (albeit on different length and time scales). While the gross features between the MD and FLASH simulations are in excellent agreement, differences at the small scales are observed likely due to the absence of physical viscosity in the FLASH calculations.

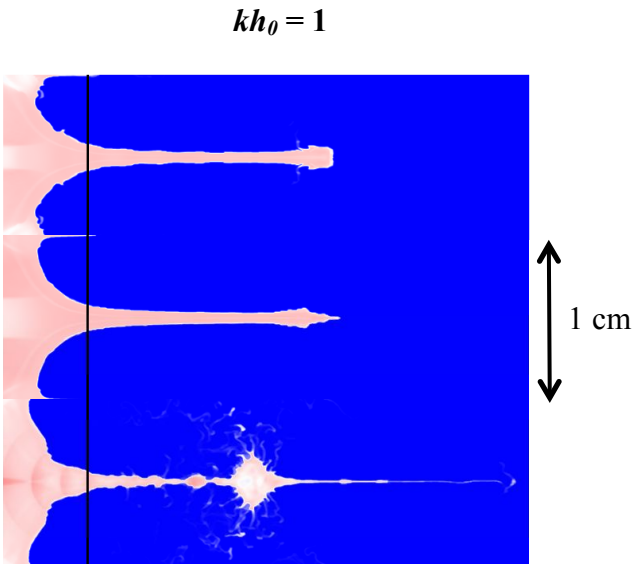

FIG. 5. FLASH simulations for Sinusoidal (upper panel), Chevron (middle panel) and Square-Wave (lower panel) shapes. kh_0=1, t/τ=16.77. Image panels correspond to (a), (b) and (d) of Fig. 4

Figure 6 shows the temporal progression of bubbles and spikes and the complex subsurface release wave structure. Figures 6 (a) – (f) show contours of density realized at key stages of flow evolution corresponding to non-dimensional times, t/τ = 0, 1.16, 6.32, 12.76, 25.62 and 51.38 respectively. The solid black line in each figure indicates the location of the equivalent free surface, obtained from a separate simulation with kh_0 = 0. The phase reversal process expected for these $A_t < 0$

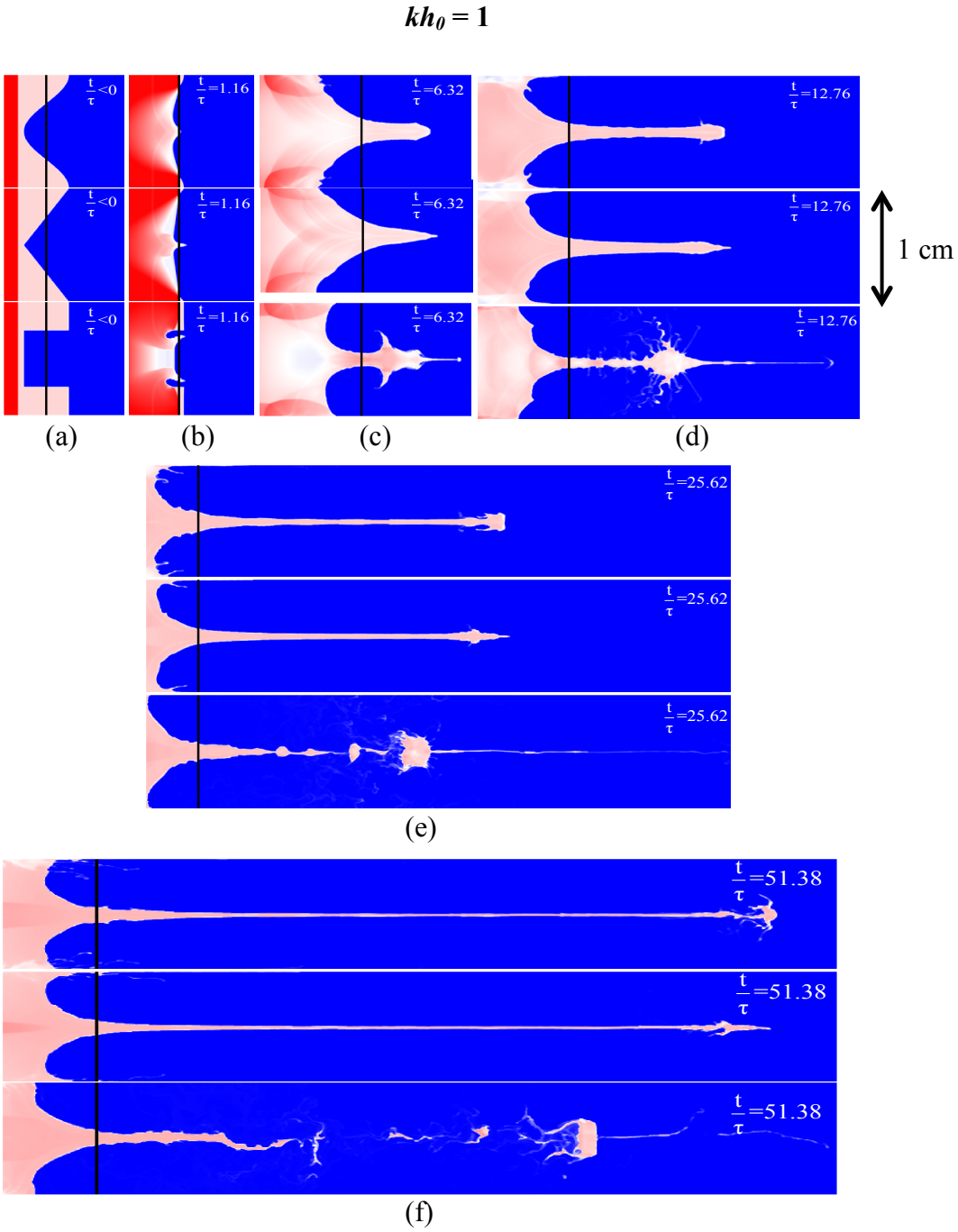

FIG. 6. FLASH simulations for Sinusoidal (upper panel), Chevron (middle panel) and Square-Wave (lower panel) shapes. kh_0=1, t/τ=0, 1.16, 6.32, 12.76, 25.62, and 51.38. Image panels correspond to (a), (b) and (d) of Fig. 4.

simulations is clearly under way by t/τ = 1.16 (Fig. 6 (b)), and is complete by t/τ = 6.32 (Fig. 6 (c)). The Sinusoidal (top panel) and Chevron waveforms (middle panel) result in qualitatively similar flow structures through intermediate (Figs. 6 (c) – (d)) and late times (Figs. (e) - (f)), since the wavenumber content of the initial conditions for each of these cases are similar.

Bubble structures that are nearly flat displace the heavy fluid into long and tenuous spikes visible in Figs. 6 (d) – (f). In contrast, simulations initialized with a square wave display more complicated structures, consistent with the presence of a broad spectrum of modes that only decay as *1/n* in Equation (26). By t/τ = 51.38, spikes growing out of a square wave perturbation appear to be susceptible to a secondary instability seen in the bottom panel of Fig. 6 (f). Note that by $t/\tau \sim 51.38$ (fig. 6f), the spikes only span a few mesh cells and are thus likely to be no longer resolved structures. Thus, the breakup seen in fig. 6f could be attributed to numerical dissipation at such small scales. Overall, the hydrodynamic simulations produce spike amplitudes that are in good agreement with the MD simulations at similar values of t/τ for the same values of kh_0 (see Figures 4 and 5). Note that at large initial amplitudes ($kh_0 = 1$), both FLASH and SPaSM simulations exhibit complex secondary features not observed at lower values of kh_0. These features include bubble-side ejections and blunted spike tips (figs. 4-6), and are attributed to the additional vorticity deposited at the interface at larger interfacial amplitudes due to the increased misalignment between the shock and the interface. Such features have been observed elsewhere in simulations[3] and pRad experiments[2]. The FLASH simulations were performed without surface tension (T) and viscosity (μ). We believe these effects may cause modifications at the fine-scale structure of the microjetting phenomena, but do not significantly affect the integral quantities discussed in this paper. For instance, surface tension has been observed to cause jet breakup and fragmentation of spikes at late times in experiments. However, the FLASH simulations reported here have been run up to $kV_0t \sim 50$ (where V_0 is the initial linear RM growth rate), a time period over which the surface tension driven breakup process does not advance significantly. This can be demonstrated with the following simple analysis adapted from [3]: The velocity scale associated with the spike fragmentation process can be written as $V_{jet-breakup} \sim \sqrt{2T/\rho_2\lambda}$ (from [46]). Using the surface tension for molten Cu (T ~ 1000 dyne/cm [47]), we obtain $V_{jet\text{-}breakup} \sim 0.03$ km/s for MD simulations, and 16.25 cm/s for FLASH simulations (if it had surface tension). For the longest simulations in this study with $kV_0t \sim 50$, the spike fragmentation process has only experienced $V_{jet-breakup} \times \frac{kV_0t}{V_0} \sim 0.63$ (~ 1.38) e-foldings[3] for the MD (FLASH) simulations (while the RMI has clearly proceeded to non-linearity). Thus, we do not expect the exclusion of surface tension in FLASH to significantly alter the results compared to its MD counterpart. Similarly, the model of [48] may be used to estimate the reduction in growth rate due to viscosity of molten Cu in the MD simulations relative to the continuum simulations, which were inviscid. From [48], in the presence of viscosity, the RM growth rate is modified according to

$$\dot{h} = h_0 \Delta u A_t k e^{\left(-2k^2\nu t\right)} \tag{32}$$

For the MD simulations, the strain rates may be determined as ~ kV_0 ~ 8.8e9 s^{-1} (5.9e10s-1) for the kh_0 = 1/8 (1) cases. Taking μ ~ 4 mPa-s for molten Cu from tabulated values in [49], we compute the growth rate reduction due to viscosity over a nonlinear timescale of kV_0t ~ 1, to be 7% (1%) for the kh_0 = 1/8 (1) simulations. Thus, we do not expect significant differences in the linear growth rates between FLASH and SPaSM. Furthermore, the strain rates in the FLASH simulations are much lower (kV_0 ~ 5.6e2 (3.7e3) s^{-1} for the kh0 = 1/8 (1) cases). It is not clear how viscosity would affect RM in the nonlinear stage, but we expect small-scale features (visible in some of the FLASH simulations) to be affected by the inclusion of viscosity.

We have used several methods to analyze the computed results. We first define an effective wavelength, λ_{eff}, from the area excavated out to form the initial surface perturbation, A_{sh}, by $\lambda_{eff} = A_{sh}/h_0$,where h_0 is the half height of the peak to valley distance. Accordingly, the effective wavenumber $k_{eff} = 2\pi/\lambda_{eff}$ and the timescale τ (Equation (3)) is given by $\tau_{eff} = \lambda_{eff} / (3\pi\dot{\eta}_0^b)$. Similarly, an effective mass per unit area m_{0eff}, can be defined as $m_{0eff} = \rho\lambda_{eff} / 3\pi$. It can be shown that upon integration of Equation (2), substituting k_{eff} in place of the k, m_0 in Equation (3) becomes m_{0eff}. We also define an amplitude h_{0f}, equal to the first amplitude coefficient in the Fourier series expansion. Tables 1 and 2 provide parameter values for the shapes considered for values of kh_0 =1 and 1/8.

We start our analysis by inspecting the areal mass vs. time plots in Figures 7a and 7c, and Figures 8a and 8c for the SPaSM and FLASH simulations respectively. Although all the shapes had the same h_0 and λ it is evident that they produce different areal masses, with the flycut being the lowest for kh_0=1/8 and the highest for kh_0=1, in both SPaSM and FLASH simulations. Our model suggests an areal mass scaling of $m_0=\rho\lambda/3\pi$. Since λ is the same for all the shapes this will not usefully scale the shapes. However, the Figures 7b and 7d, Figures 8b and 8d show that a scaling based on $m_{0eff}=\rho\lambda_{eff}/3\pi$ does give a useful collapse for both kh_0=1 and 1/8. This is essentially the same scaling used by Asay and Bertholf[1]. However our model suggests an additional time scaling is necessary, and this is examined in the next paragraph.

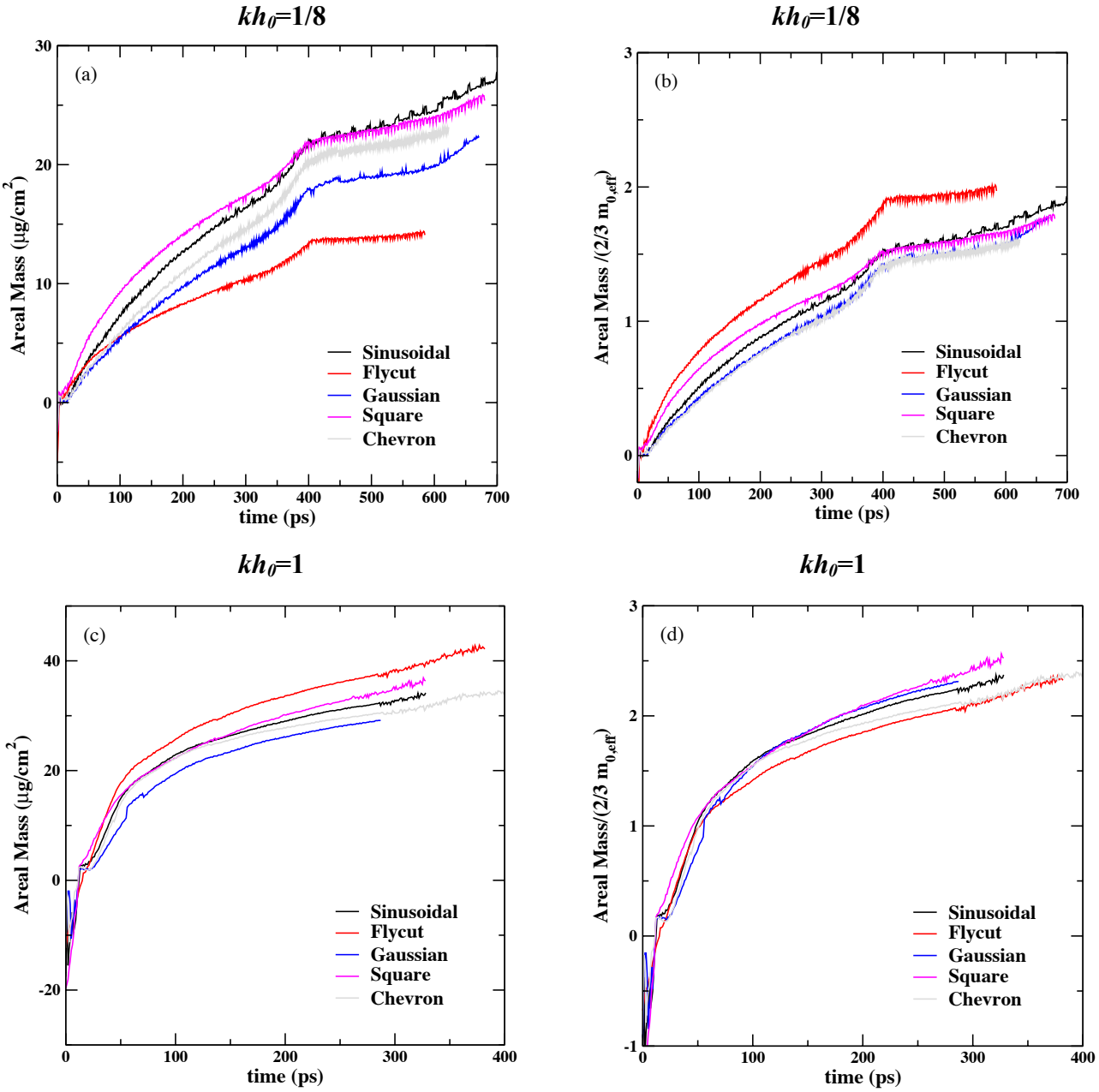

FIG. 7. Ejected mass per unit area for vs. time. SPaSM simulations, u_p=2.5 km/s, P=161 GPa. Initial temperature 300 K. a) kh_0=1/8, $m(t)$ vs. time; b) kh_0=1/8, scaled mass $m(t)/(2/3m_{0eff})$ vs. time; c) kh_0=1, m(t) vs. time; d) kh_0=1, scaled mass $m(t)/(2/3m_{0eff})$ vs. time.

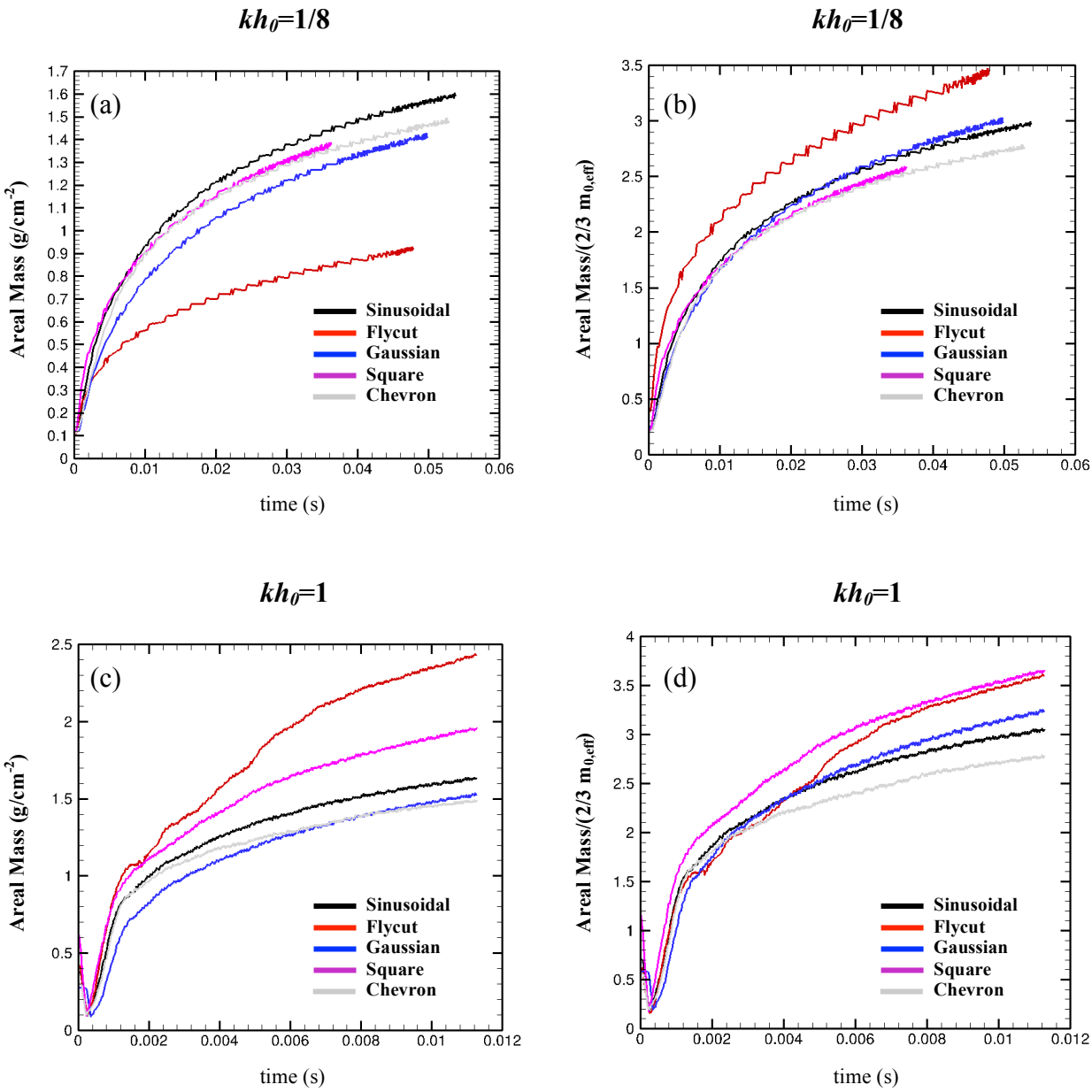

FIG. 8. Ejected mass per unit area for FLASH simulations. a) kh_0=1/8, $m(t)$ vs. time; b) kh_0=1/8, scaled mass $m(t)/(2/3m_{0eff})$ vs. time; c) kh_0=1, $m(t)$ vs. time; d) kh_0=1, scaled mass $m(t)/(2/3m_{0eff})$ vs. time.

To further assess the model given in Equations (9) and (12) it is necessary to specify τ_{eff}, which depends on both λ and kh_0. We consider two methods. The first method (I) assumes that a shape with a given peak to valley height $2h_0$, may be represented by an equivalent sinusoidal perturbation with $\lambda \rightarrow \lambda_{eff}$ and $kh_0 \rightarrow k_{eff} h_0$. The second method (II) assumes that at

late times, the bubble growth is dominated by the longest wavelength in the Fourier decomposition as discussed above. We thus take λ and $kh_0 \rightarrow kh_{0f}$ as variables in Equation (9). Figures 9 and 10 compare these two methods for the MD simulations (Figure 9) and the FLASH hydrodynamic simulations (Figure 10). Figures 9a and 9c show the ejecta mass per unit area scaled by 2/3 m_{0eff} plotted vs. the natural logarithm on the right hand side of Equation (9) using method (I). Figure 9a corresponds to kh_0=1/8 and Figure 9c to kh_0=1. Figures 9b and 9d are the same kh_0 values using method (II). Figures 10a – 10d are the same as for Figure 9 but for the FLASH simulations. The break in slope seen in Figures 9a, 9b, 7a, and 7b (kh_0=1/8) is due to the reflected rarefaction wave from the back surface reaching the interface. This has not occurred for the shorter run times in Figures 9c, 9d, 7c, and 7d (kh_0=1). The FLASH simulations were run for approximately 12 milliseconds for kh_0=1 cases ($t/\tau \sim 65$), and 54 milliseconds for kh_0=1/8 cases ($t/\tau \sim 44$). Perfect agreement between theory and simulation corresponds to a straight line at 45^o in these figures. We track independently the time evolution of bubble and spike tips in both SPaSM and FLASH simulations, from which we obtain the timestamps of the following key events: the instance when the shock first arrives at the interface (T_1), the time instance when the shock arrives at the peak of the perturbation (T_2), and the instance when the interface is flat (T_3). Δt is then computed as $\Delta t = T_3 - T_1$ for use in eq. (9).

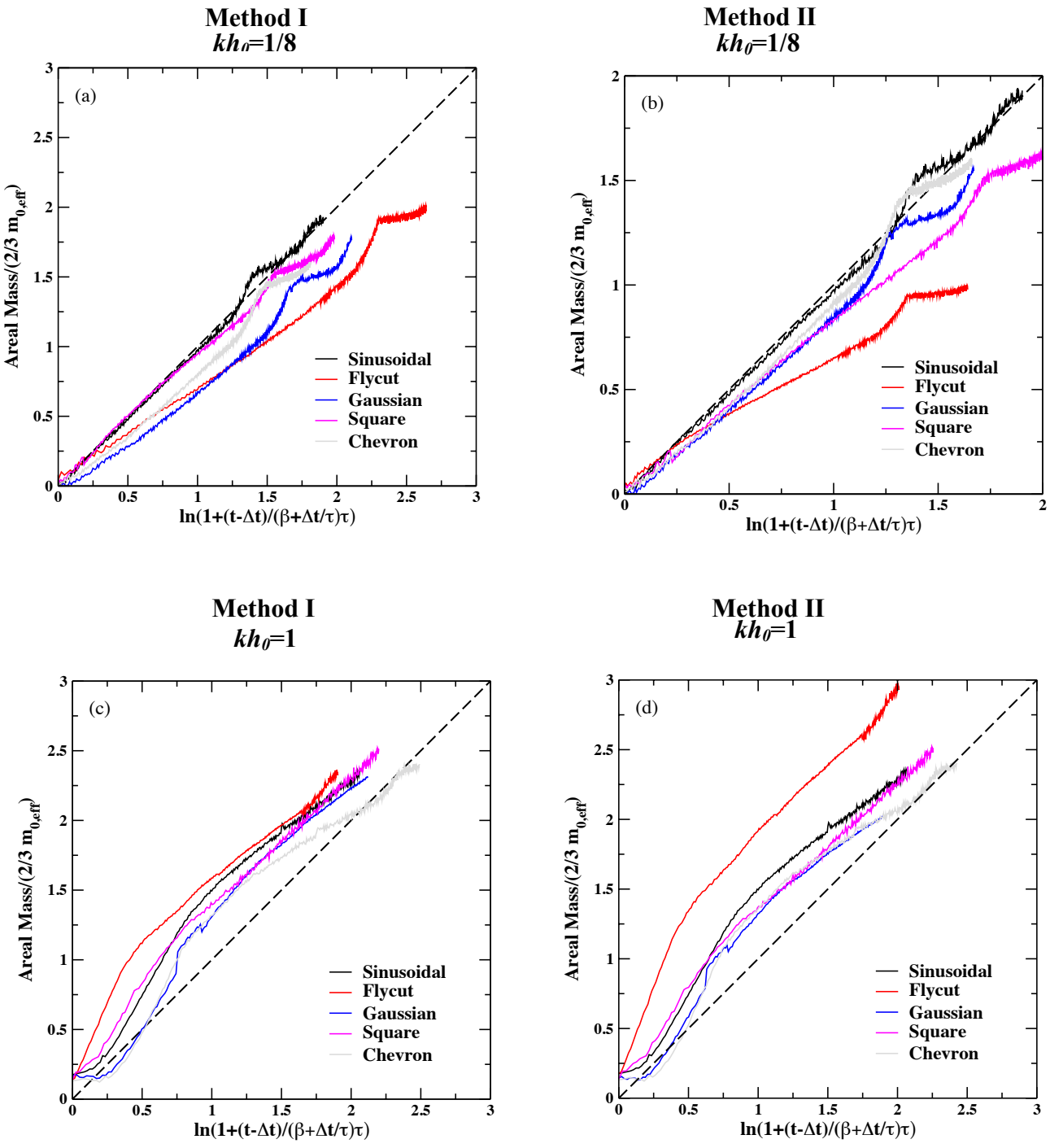

Figure 9. Simulation mass per unit area compared with theoretical model, SPASM simulations. (a) and (b) kh_0=1/8: (a) – Method I , (b) – Method II ; (c) and (d) kh_0=1: (c) – Method I , (d) – Method II. Dashed line – theoretical model.

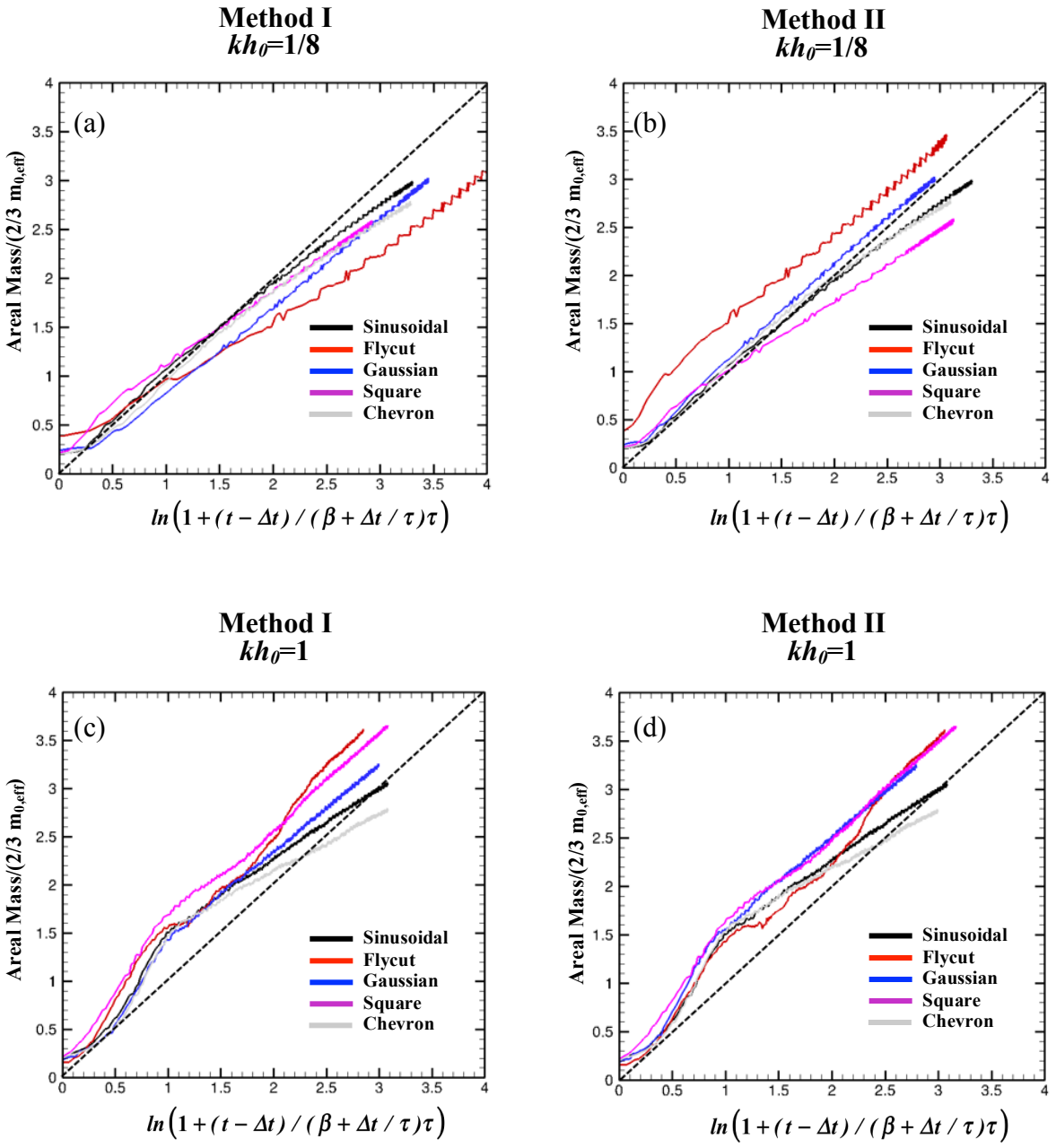

FIG. 10. Simulation mass per unit area compared with theoretical model, FLASH simulations. (a) and (b) kh_0=1/8: (a) – Method I , (b) – Method II ; (c) and (d) kh_0=1: (c) – Method I , (d) – Method II. Dashed line – theoretical model.

Comparison of Figures 9 with 10 reveals a reasonable agreement with the theoretical prediction using both method I and II. However one must take into account the scaling of the data and ordering of the curves shown in Figures 7 and 8. Referring to tables 1 and 2, the ordering in figures 7a, 7c, 8a, and 8c has the highest areal mass corresponding to the largest values of λ_{eff}. When λ_{eff} is the same, the ordering is approximately according to the magnitude of h_{0f}. Method I incorporates the λ_{eff} ordering explicitly in the pre-factor m_{0eff}. Since method I depends on the local geometry of the perturbation it may be useful for calculating the ejected mass from machined surfaces with local inhomogeneities and a distribution of surface roughness. Method II incorporates the missing area dependence in τ_{eff} through h_{0f} rather than with λ_{eff} and gives areal masses proportional to h_{0f} in the limit that $t \ll \tau$ which is approximately correct for the simulation data. We recommend method I because of its simplicity and its ease of generalization to non-periodic or quasi-periodic surface profiles. In Figures 9c and 9d, 10c and 10d, for $t^*<1$ (where $t^* = ln\left(1+(t-\Delta t)/(\beta+\Delta t/\tau)\tau\right)$) and $kh_0=1$ there is a steeper growth of areal mass release, but thereafter the areal mass release matches well with the model. This steeper release for $kh_0=1$ does not occur for $kh_0=1/8$ indicating that the initial inversion period does not follow the sinusoidal path suggested by the model collapse. However, the $t^*>1$ collapse for $kh_0=1$ onto the model supports the overarching hypothesis that late-time areal mass release is controlled by the longest wavelength and initial amplitude.

VI. CONCLUSIONS

We have presented a source model for the production of ejecta at a shocked interface for which the release state of the material is a fluid. The model takes into account the details of non-sinusoidal shapes in the context of a Richtmeyer-Meshkov instability. The main results for the model are Equations (9) and (12). It depends on a scaled wavelength and volume (mass) conservation for bubble and spike growth and is readily generalized to multiple shock impacts. The model correctly predicts the time dependence of the areal mass over length scales from nm to cm and is predictive for quasi two-dimensional machined surfaces when the surface topography is known.

Two variants for the magnitude of the ejected mass per unit area have been considered and compared with detailed simulations at atomistic and macroscopic scales using the SPaSM non-equilibrium molecular dynamics code and the FLASH hydrodynamics code. These two model variants both account reasonably well for the magnitude and time dependence of the ejected mass. One (method I) incorporates local shape through an effective wavelength, λ_{eff}, defined by the local geometry of the surface defect structure. A second (method II) incorporates shape through the first coefficient of the Fourier expansion giving an effective amplitude. Both methods assume that the late time bubble development is dominated by the longest wavelength, an assumption that is corroborated by the simulation results presented here. The model also accounts for the

time-dependent shape of the ingrowing bubble which gives rise to a reduction in ejected mass in the form of a pre-factor of 2/3.

The model gives a good accounting of the magnitude and time dependence when compared with simulations for a supported shock wave over a range of length scales from nm to cm, and time scales from ps to ms. The extension to multiple shock waves was discussed, under the reasonable assumption that the longest wavelength is retained, and that the new amplitude is ½ the bubble amplitude at the time of second and subsequent shock breakout. The present model serves as a useful baseline for future extensions that might include spike breakup, shock shape, and subsurface damage. We close by noting that the model has been cast in a form (Equation 12) that can be readily implemented in hydrodynamic codes.

ACKNOWLEDGMENTS

This work was supported in part by the (U.S.) Department of Energy (DOE) under Contract No. DE-AC52-06NA2-5396. PR and VK acknowledge the Texas Advanced Computing Center (TACC) at The University of Texas at Austin for providing HPC resources, and computer time awarded under the NSF Teragrid program. FLASH was developed by the DOE-sponsored ASC/Alliance Center for Astrophysical Thermonuclear Flashes at the University of Chicago.

REFERENCES

[1]J. R. Asay and L. D. Bertholf, Tech. Rep. SAND78-1256, Sandia National Laboratories (1978).

[2]W. T. Buttler, D. M. Oró, D. L. Preston, K. O. Mikaelian, F. J. Cherne, R. S. Hixson, F. G. Mariam, C. Morris, J. B. Stone, G. Terrones, et al., J. Fluid Mech. **703**, 60 (2012).

[3]G. Dimonte, G. Terrones, F. J. Cherne, and P. Ramaprabhu, J. Appl. Phys. **113**, 024905 (2013).

[4]K. O. Mikaelian, Phys. Fluids **17**, 034101 (2005).

[5]W. S. Vogan, W. W. Anderson, M. Grover, J. E. Hammerberg, N. S. P. King, S. K. Lamoreaux, G. Macrum, K. B. Morley, P. A. Rigg, G. D. Stevens, et al., J. Appl. Phys. **98**, 113508 (2005).

[6]M. B. Zellner, M. Grover, J. E. Hammerberg, R. S. Hixson, A. J. Iverson, G. S. Macrum, K. B. Morley, A. W. Obst, R. T. Olson, J. R. Payton, et al., J. Appl. Phys. **102**, 013522 (2007).

[7]M. B. Zellner, W. Vogan-McNeil, G. T. Gray III, D. C. Huerta, N. S. P. King, G. E. Neal, S. J. Valentine, J. R. Payton, J. Rubin, G. D. Stevens, et al., J. Appl. Phys. **103**, 083521 (2008).

[8]M. B. Zellner, M. Grover, J. E. Hammerberg, R. S. Hixson, A. J. Iverson, G. S. Macrum, K. B. Morley, A. W. Obst, R. T. Olson, J. R. Payton, et al., J. Appl. Phys. **103**, 109901 (2008).

[9]M. B. Zellner, W. Vogan-McNeil, J. E. Hammerberg, R. S. Hixson, A. W. Obst, R. T. Olson, J. R. Payton, P. A. Rigg, N. Routley, G. D. Stevens, et al., J. Appl. Phys. **103**, 123502 (2008).

[10]M. B. Zellner and W. T. Buttler, Appl. Phys. Lett. **93**, 114102 (2008).

[11]W. T. Buttler, M. B. Zellner, R. T. Olson, P. A. Rigg, R. S. Hixson, J. E. Hammerberg, A. W. Obst, J. R. Payton, A. Iverson, and J. Young, J. Appl. Phys. **101**, 063547 (2007).

[12]A. B. Georgievskaya and V. A. Raevsky, AIP Conference Proceedings **1426,** 1007 (2012).

[13]A. L. Mikhailov, V. A. Ogorodnikov, V. S. Sasik, V. A. Raevsky, A.I. Lebedev, D. E. Zotov, S. V. Erunov, M. A. Si'runin, V. D. Sadunov, N. V. Nevmershitsky, S. A. Lobastov, V. V. Burtsev, A. V. Mishanov, E. V. Kulakov, A. V. Satarova, A. B. Georgievskaya, V. N. Knyazev, O. A. Klewevnikov, M. V. Antipov, V. V. Glushihin, I. V. Yurtov, A. A. Utenkov, E. D. Sen'kovsky, S. A. Abakumov, D. V. Presnyakov, I. A. Kalashnik, K. N. Panov, V. A. Arinin, B. I. Tkachenko, V. N. Filyaev, A. V. Chapaev, A. V. Andramanov, M. O. Lebedeva, V. V. Igonin, J. Expt. And Theor. Phys. **118,** 785 (2014).

[14]O. Durand and L. Soulard, J. Appl. Phys. **114,** 044901 (2012).

[15]O. Durand and L. Soulard, J. Appl. Phys. **114,** 194902 (2013).

[16]J.-L. Shao, P. Wang, A.-M. He, S.-Q. Duan, and C.-S. Qin, J. Appl. Phys. **113,** 153501 (2013).

[17]J.-L. Shao, P. Wang, and A.-M. He, J. Appl. Phys. **116,** 073501 (2014).

[18]G. Ren, Y. Chen, T. Tang, and Q. Li, J. Appl. Phys. **116,** 133507 (2014).

[19]B. Li, F. P. Zhao, H. A. Wu, and S. N. Luo, J. Appl. Phys. **115,** 073504 (2014).

[20]O. Durand and L. Soulard, J. Appl. Phys. **117,** 165903 (2015).

[21]T. C. Germann, J. E. Hammerberg, and B. L. Holian, AIP Conference Proceedings **706**, 285 (2004); T. C. Germann, G. Dimonte, J. E. Hammerberg, K. Kadau, J. Quenneville, and M. B. Zellner, DYMAT 2009, EDP Sciences, 1499 (2009).

[22]S. V. Zybin, V. V. Zhakhovskii, E. M. Bringa, S. I. Abarzhi, and B. Remington, AIP Conference Proceedings **845**, 437 (2006).

[23]B. L. Holian and P. S. Lomdahl, Science **280**, 2085 (1998).

[24]K. Kadau, T. C. Germann, P. S. Lomdahl, and B. L. Holian, Science **296**, 1681 (2002).

[25]E. M. Bringa, J. U. Cazamias, P. Erhart, J. Stolken, N. Tanushev, B. D. Wirth, R. E. Rudd, and M. J. Caturla, J. Appl. Phys. **96**, 3793 (2004).

[26]J. W. Mintmire, D. H. Robertson, and C. T. White, Phys. Rev. B **49**, 14859 (1994).

[27]P. Erhart, E. M. Bringa, M. Kumar, and K. Albe, Phys. Rev. B **72**, 052104 (2005).

[28]A. Strachan, T. Cagin, and W. A. Goddard, Phys. Rev. B **63**, 060103 (2001).

[29]K. O. Mikaelian, Phys. Rev. Let. **80**, 508 (1998).

[30]K. O. Mikaelian, Phys. Rev. E **81**, 016325 (2010).

[31]K. Kadau, T. C. Germann, N. G. Hadjiconstantinou, P. S. Lomdahl, G. Dimonte, B. L. Holian, and B. J. Alder, Proc. Natl. Acad. Sci. USA 101, 5851-5855 (2004).

[32]K. Kadau, C. Rosenblatt, J. L. Barber, T. C. Germann, Z. Huang, P. Carles, and B. J. Alder, Proc. Natl. Acad. Sci. USA 104, 7741-7745 (2007).

[33]M. S. Daw and M. I. Baskes, Phys. Rev. Lett. **50**, 1285 (1983).

[34]M. S. Daw and M. I. Baskes, Phys. Rev. B **29**, 6443 (1984).

[35]A. F. Voter, Tech. Rep. LA-UR-93-3901, Los Alamos National Laboratory (1993).

[36]A. F. Voter, Phys. Rev. B 57, 13985 (1998).

[37]F. J. Cherne, G. Dimonte, and T. C. Germann, AIP Conference Proceedings **1426**, 1307 (2012).

[38]D. Hayes, R. S. Hixson, and R. G. McQueen, AIP Conference Proceedings **505**, 483 (2000).

[39]P. S. Lomdahl, P. Tamayo, N. G. Jensen, and D. M. Beazley, in *Proceedings of Supercomputing '93*, edited by G. S. Ansell (IEEE Computer Society Press, Los Alamitos, CA, 1993), 520.

[40]D. M. Beazley and P. S. Lomdahl, Computers in Physics **11**, 230 (1997).

[41]K. Kadau, T. C. Germann, and P. S. Lomdahl, Int. J. Mod. Phys. C. **17**, 1755 (2006).

[42]B. Fryxell, K. Olson, P. Ricker, F. Timmes, M. Zingale, D. Lamb, P. MacNeice, R. Rosner, J. Truran and H. Tufo, Astrophys. J., Suppl. Ser. **131**, 273 (2000).

[43]P. Colella and P. R. Woodward, J. Comput. Phys. **54**, 174-201 (1984).

[44]K. O. Mikaelian, Phys. Fluids **6**, 356 (1994).

[45]N. N. Mansour and T. S. Lundgren, Phys. Fluids A **2**, 1141 (1990).

[46]E. B. Webb and G. S. Grest, Phys. Rev. Lett. **86**, 2066 (2001).

[47]K.O. Mikaelian, Phys. Rev E, **47**, 375 (1993).

[48]M. J. Assael et al., J. Phys. Chem. Ref. Data, **39**, 33105 (2010).

TABLE Ia. SPaSM MD Simulations: kh_0=1/8, h_0=5.1129 nm, λ=257 nm.

Shape	h_{0f} (nm)	λ_{eff} (nm)	k_{eff} (nm^{-1})
Sinusoidal	5.1129	257	0.02445
Flycut	4.4197	127	0.04924
Gaussian	3.7362	225	0.03683
Square	6.5099	257	0.02445
Chevron	4.1443	257	0.02445

TABLE Ib. SPaSM MD Simulations: kh_0=1.0, h_0=40.9028 nm, λ=257 nm.

Shape	h_{0f} (nm)	λ_{eff} (nm)	k_{eff} (nm^{-1})
Sinusoidal	40.9028	257	0.02445
Flycut	39.0461	323	0.02285
Gaussian	29.8898	225	0.02445
Square	52.0791	257	0.02445
Chevron	33.1546	257	0.02445

TABLE IIa. FLASH Simulations: kh_0=1/8, h_0=0.02 cm, λ=1.0 cm.

Shape	h_{0f} (cm)	λ_{eff} (cm)	k_{eff} (cm^{-1})
Sinusoidal	0.02	1.0	6.2832
Flycut	0.0173	0.5	12.5664
Gaussian	0.0146	0.88	7.1400
Square	0.0255	1.0	6.2832
Chevron	0.0162	1.0	6.2832

TABLE IIb. FLASH Simulations: kh_0=1.0, h_0=0.1592 cm, λ=1.0 cm.

Shape	h_{0f} (cm)	λ_{eff} (cm)	k_{eff} (cm^{-1})
Sinusoidal	0.1592	1.0	6.2832
Flycut	0.1519	1.26	4.9867
Gaussian	0.1163	0.88	7.1400
Square	0.2027	1.0	6.2832
Chevron	0.1290	1.0	6.2832